

XPOL-III: a New-Generation VLSI CMOS ASIC for High-Throughput X-ray Polarimetry

Minuti M.^a, Baldini L.^{b,a}, Bellazzini R.^a, Brez A.^a, Ceccanti M.^a, Krummenacher F.^c, Latronico L.^d, Lucchesi L.^a, Manfreda A.^a, Orsini L.^a, Pinchera M.^a, Profeti A.^a, Sgrò C.^a, Spandre G.^a

^a*Istituto Nazionale di Fisica Nucleare, Sezione di Pisa, Largo B. Pontecorvo 3, I-56127 Pisa, Italy*

^b*Università di Pisa, Dipartimento di Fisica Enrico Fermi, Largo B. Pontecorvo 3, I-56127 Pisa, Italy*

^c*Advanced Silicon SA, Lausanne, Switzerland*

^d*Istituto Nazionale di Fisica Nucleare, Sezione di Torino, Via P. Giuria, 1, I-10125 Torino, Italy*

Abstract

While the successful launch and operation in space of the Gas Pixel Detectors onboard the PolarLight cubesat and the Imaging X-ray Polarimetry Explorer demonstrate the viability and the technical soundness of this class of detectors for astronomical X-ray polarimetry, it is clear that the current state of the art is not ready to meet the challenges of the next generation of experiments, such as the enhanced X-ray Timing and Polarimetry mission, designed to allow for a significantly larger data throughput.

In this paper we describe the design and test of a new custom, self-triggering readout ASIC, dubbed XPOL-III, specifically conceived to address and overcome these limitations. While building upon the overall architecture of the previous generations, the new chip improves over its predecessors in several, different key areas: the sensitivity of the trigger electronics, the flexibility in the definition of the readout window, as well as the maximum speed for the serial event readout. These design improvements, when combined, allow for almost an order of magnitude smaller dead time per event with no measurable degradation of the polarimetric, spectral, imaging or timing capability of the detector, providing a good match for the next generation of X-ray missions.

Keywords: X-ray polarimetry

PACS: 95.55.Ka, 95.55.Qf

1. Introduction

The recent launches of the PolarLight cubesat [1] and the Imaging X-ray Polarimetry Explorer (IXPE) [2] signal the re-opening of a new observational window—that of astronomical X-ray polarimetry—after almost 40 years. At the heart of both missions are innovative polarization-sensitive Gas Pixel Detectors (GPD) [3], exploiting the photoelectric effect to derive the linear polarization of the incoming radiation based on the reconstruction of the azimuthal direction of emission of the photo-electrons. The design, qualification and successful operation in space of the PolarLight and IXPE Gas Pixel Detectors mark the culmination of a long R&D program [4, 5, 6], following the first pioneering attempts at a practical implementation of photoelectric X-ray polarimetry (see, e.g., [7]).

Future X-ray missions will pose even tighter requirements on focal-plane detectors. With a much larger effective area (about a factor $\times 5$ compared to IXPE) the mirror modules of the Polarimetry Focusing Array (PFA) onboard the enhanced X-ray Timing and Polarimetry (e-XTP) mission [8] will produce too large of a data throughput for the current generation of Gas Pixel Detectors, even for moderately bright sources. It is then clear that a drastic reduction of the dead-time per event is one of the necessary preconditions for a significant leap in sensitivity for the next generation of polarimetric missions.

In this paper we describe XPOL-III, a new-generation custom CMOS ASIC specifically designed for high-throughput X-ray polarimetry applications, taking full advantage of the lessons

learned through the development of the IXPE mission. The new design is specifically aimed at a substantial reduction of the average dead time per event, while preserving all the other relevant high-level performance metrics of the readout chip. As detailed in section 5, the first comprehensive test campaign that we performed on the new ASIC confirms that all design goals were met, and XPOL-III is a prime candidate to provide polarimetric capabilities to future X-ray missions.

2. XPOL-III Architecture

The main features of the previous XPOL generations, most of which are also relevant in the context of this work, are thoroughly described in [5, 6] and [3]. In this section we only provide a succinct summary of the internal functioning of the chip, with emphasis on the design changes specific to XPOL-III.

Parameter	Value
Number of pixels	107 008 (304 \times 352)
Physical pitch	50 μm
Shaping time	1 μs
Pixel gain	200 mV fC ⁻¹
Pixel Noise	30 e ⁻ ENC
Full scale linear range (FSLR)	30k e ⁻
Minimum trigger threshold	$\sim 150 e^-$ (0.5% of FSLR)

Table 1: Summary table of the basic geometrical and electrical characteristics of the XPOL-III readout ASIC.

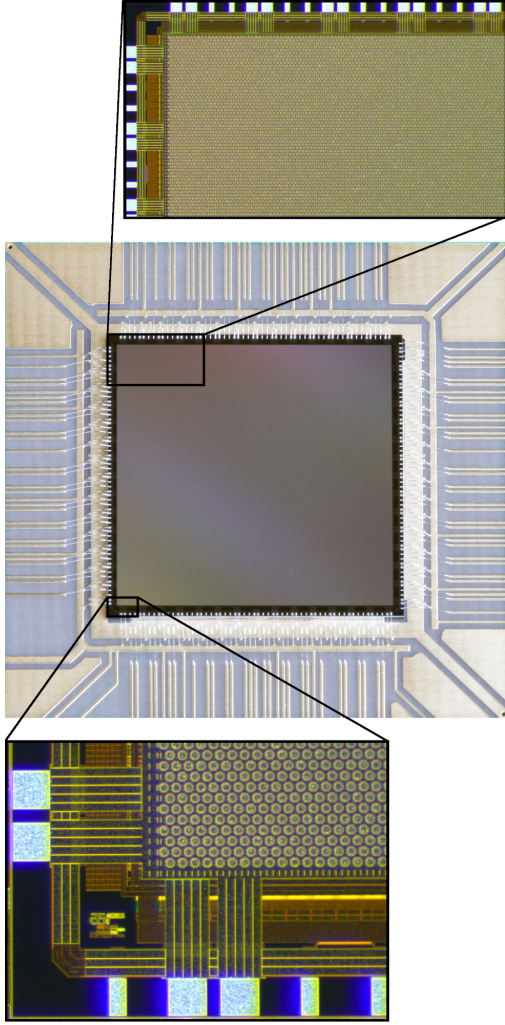


Figure 1: Picture of a XPOL-III chip (center panel), glued and wire-bonded onto its printed circuit board. The insets show micro-photographs of two of the corners at different magnification levels, with the triangular structure of the pixel array clearly visible in the bottom panel.

Manufactured with a standard 180 nm CMOS process, the XPOL-III readout ASIC (shown in Figure 1) is organized as a rectangular matrix of 107 008 hexagonal pixels arranged in a triangular pattern of 304 columns and 352 rows at $50\ \mu\text{m}$ pitch, for a total active area of $15.2 \times 15.2\ \text{mm}^2$. Each pixel is composed of a metal electrode (from the top layer of the process), acting as a charge-collecting anode, connected to a charge-sensitive amplifier, followed by a shaping circuit and a sample-and-hold system, as illustrated in the simplified schematic in Figure 2.

Similarly to the previous ASIC generations, XPOL-III provides an advanced self-triggering capability, with automatic localization of the *region of interest* (ROI) containing the photoelectron track. Upon trigger, the outputs of the pixels within the ROI are sequentially connected to an on-chip global differential amplifier driving the output pads, and the digitization of the corresponding signal is performed with a dedicated, external ADC. At a very fundamental level, this is the basic mechanism that allows to keep the overall readout time manageable, as, for a typical event, we only read out a few hundreds pixels

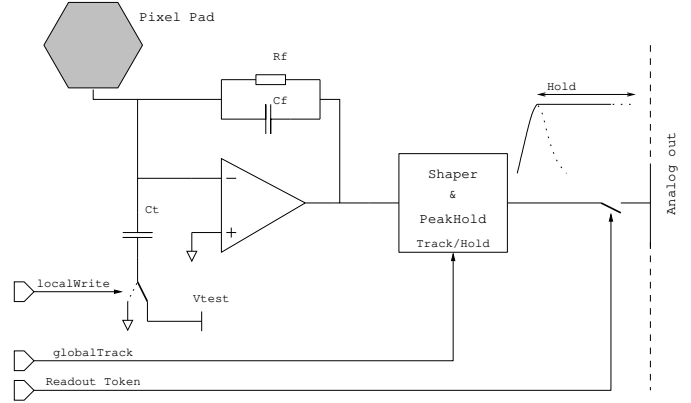


Figure 2: Simplified pixel schematic.

out of the $> 100\ \text{k}$ in the full matrix. Building on this concept, in the initial stages of the XPOL-III design we identified three distinct possible lines of actions to speed up the readout:

- reduce the average size of the region of interest;
- increase the maximum frequency of the serial readout clock;
- streamline the readout sequence to avoid unnecessary delays.

As we shall discuss in the remaining of this section, the combination of these three, seemingly simple updates provides a drastic dead-time reduction.

2.1. Event Triggering

Every 4 pixels in the ASIC are logically OR-ed together to contribute to a local trigger with a dedicated shaping amplifier. This basic building block of 2×2 pixels is called a trigger *mini-cluster*, and is central to the entire trigger logic. Upon trigger, the event is automatically localized by the ASIC core logic in the smallest rectangle containing all triggered mini-clusters, called the *region of trigger* (ROT). More specifically, the chip calculates and makes available in a specific register the coordinates $\langle X_{\min}, Y_{\min} \rangle$ and $\langle X_{\max}, Y_{\max} \rangle$ of the upper-left and lower-right corners of the ROT. On an event by event basis, this information can be manipulated in an arbitrary fashion—typically by adding a pre-defined padding on the four borders—to define the *region of interest* (ROI) for the event capture and readout.

While the top-level trigger logic in the previous generations of the ASIC was similar to that of XPOL-III, the algorithm implemented in XPOL-I to define the ROI was comparatively crude: a constant padding of 8 columns on the left and right and 10 rows on the top and bottom of the ROT was automatically added by the ASIC, as shown in Figure 3, with no room for additional tuning. This approach served well the primary purpose of making the ROI big enough to fully contain the tracks at all the energies of interest (and was ultimately adequate for the typical IXPE throughput), but was clearly sub-optimal at low energy, where tracks tend to be more compact and with a comparatively higher ionization density.

In contrast, XPOL-III offers maximal flexibility—to the point that, once the ROT has been defined by the ASIC, the ROI

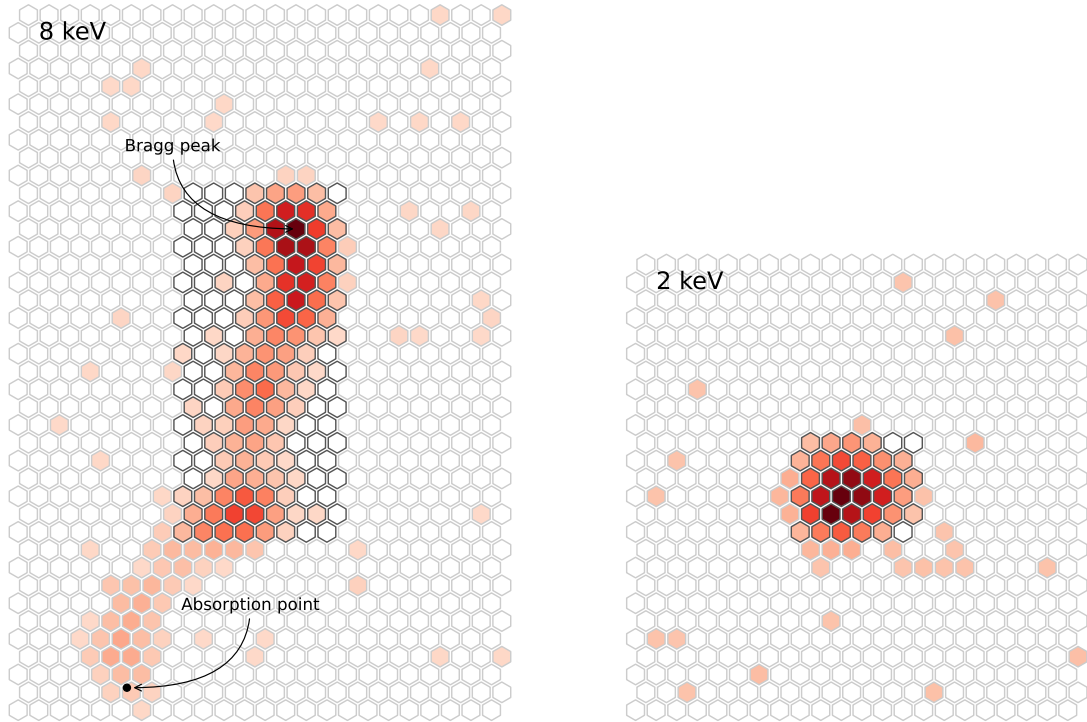


Figure 3: Sample simulated photo-electron tracks at 8 keV (left) and 2 keV (right) in pure DME at 800 mbar, embedded in the respective XPOL-I-like readout windows at the nominal trigger threshold. Pixels are depicted with black and gray borders depending on whether they lie within the ROT or the outer padding region (8 columns on the left and the right of the ROT and 10 rows on the top and the bottom). As illustrated in the left panel, this comparatively large padding is necessary in the XPOL-I setup in order to guarantee that the initial part of high-energy tracks is fully contained in the ROI, but is largely sub-optimal on the low-end of the spectrum, where tracks are much more compact. With a significantly lower trigger threshold and a more flexible padding strategy, XPOL-III is capable of generating much smaller ROIs without compromising the track containment.

can be calculated by means of any arbitrary external logic and loaded into the proper register on an event-event-basis. Additionally, a *hybrid* operational mode is available where a pre-loaded padding, independently adjustable on the four sides of the ROT, is automatically applied by the chip without the need of an additional data transactions. (In practice, since the information available at the time that the ROI decision has to be made is limited, this hybrid mode is in fact outperforming overly sophisticated padding schemes, and will be the baseline configuration used for all the tests described in the following of the paper.) Even more importantly, this additional flexibility in the definition of the ROI is accompanied by another fundamental design change: the AC nature of the XPOL-III trigger coupling. Compared to the XPOL-I architecture, where the dispersion of the DC offsets across different amplifiers was playing a prominent role, this change allows to lower dramatically the minimum trigger threshold practically achievable, increasing, in turn, the fraction of mini-clusters in the track participating in the trigger.

It cannot be over-emphasized that these two seemingly simple changes in the trigger circuitry constitute a change of paradigm and a radical departure from how previous iterations of the ASIC operated. To put things in the simplest possible way, in XPOL-I it was mostly the Bragg peak to participate into the trigger, and we had to resort to a comparatively large padding of the ROT in order to capture the initial part of the high-energy tracks. In

XPOL-III the entire track participates into the trigger at all energies, and a minimal additional padding is sufficient to ensure full containment of the track. As shown in Figure 4, this allows for ROIs that are smaller on average, and scale more favorably with the track length, offering additional leverage for the operation at the focus of a X-ray optics, where the vast majority of the photons are detected at the lower end of the energy spectrum. Assuming a constant padding of 2 (4) pixels on all four sides of the ROT, the XPOL-III design results in an overall reduction of the ROI size by a factor of 3.5 (2), across the band.

2.2. Event Readout and Pedestal Subtraction

Upon trigger, in nominal data-taking configuration, the chip autonomously initiates the peak-detection process of the internal sample-and-hold system, at the end of which the analog output of each pixel within the ROI is sequentially routed to the differential output buffer connected to the external ADC, and the serial readout proceeds driven by an adjustable readout clock provided by the back-end electronics. The region of interest is actually read out twice, and the FPGA on the DAQ board then performs the pixel-by-pixel pedestal subtraction and proceeds to the zero suppression and the event compression and transmission [9]. As explained in [3], this online pedestal subtraction is useful to minimize subtle systematic effects that were found to be important for our application.

While a detailed technical description of the readout sequence is beyond the scope of this paper, the readout time per

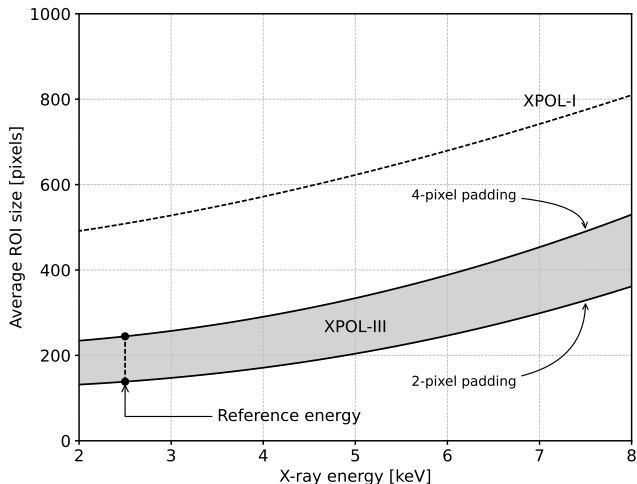


Figure 4: Average ROI size as a function of the X-ray energy for XPOL-I and XPOL-III (in the latter case, with a constant padding of 2 and 4 pixels on all four sides of the ROT). As we shall see in section 4, the shaded region between the two solid lines is the useful phase space for determining the optimal working point. For reference, at 2.5 keV (which is germane to the IXPE peak sensitivity), XPOL-III yields an average ROI size comprised between 140 and 240 pixels, at the two different padding settings, which is 3.5–2 times smaller than the XPOL-I equivalent.

event can be parametrized, neglecting sub-dominant contributions, as a linear function of the number of pixels n_{pix} in the region of interest

$$T_{read} = q + mn_{pix}, \quad (1)$$

where the constant term q incorporates, e.g., the peak-detection interval, the necessary data transactions to execute the readout and reset the system, as well as all the fixed delays that are needed to synchronize the sequence, while the slope m captures all the contributions whose duration is proportional to the size of the ROI, such as the event serial readout sequence and the pedestal subtraction in FPGA. (We note that both q and m depend on the particular settings of the readout ASIC and the back-end electronics with, e.g., m being dominated by the serial readout clock.)

Compared to XPOL-I, much of the differential output has been redesigned in XPOL-III in order to streamline the readout. The design of the output buffer has been tuned to minimize the settling time of the analog signal and increase the maximum serial readout clock practically usable, which for XPOL-I was limited to ~ 5 MHz, and the analog reset circuitry has been reworked to avoid the need for extra delays, necessary in XPOL-I to avoid self-induced false triggers. One additional notable change is that the ROI coordinates, once determined, remain stored in their register until the latter is explicitly reset, which avoids another class of fixed delays necessary in XPOL-I to perform the online pedestal subtraction. The net result of all these optimization is a net (and significant) reduction of both terms in Equation (1), as we shall see in section 4.

3. Measurement setup

The GPD assembly is the natural *packaging* for the readout ASIC, and an essential ingredient for testing its functionality beyond the basic electrical aliveness. We have assembled, baked-out, filled and sealed entirely in house, a few detectors equipped with a XPOL-III readout ASIC. Figure 5 shows an exploded view of the detector, whose design implements some important simplification with respect to the focal plane detectors onboard IXPE [3].

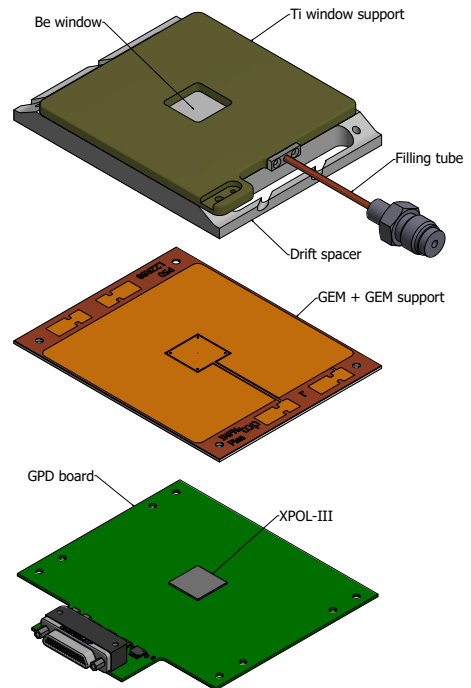


Figure 5: Exploded view of a GPD equipped with a XPOL-III readout ASIC. The main differences with respect to the models used in IXPE are the chip-on-board configuration and the absence of the internal aluminization of the Be foil.

We kept the top-level geometry and gas mixture, but we opted for a chip-on-board scheme (i.e. with the ASIC directly glued and wire-bonded over its printed circuit board, avoiding the use of a ceramic package) to simplify the assembly. We used $50 \mu\text{m}$ pitch, $50 \mu\text{m}$ thick GEM foils manufactured with a conventional chemical etching process. Finally, the entrance window is a simple $50 \mu\text{m}$ Be foil with no aluminization. The main characteristics of the detectors are summarized in table 2.

Each one of these modifications is a step toward our ultimate goal of a new-generation Gas Pixel Detector, featuring a simpler and more robust mechanical assembly, and a higher polarization sensitivity—both in terms of modulation factor and uniformity of response to unpolarized radiation. A detailed description of the GPD development, including the description of a dedicated filling facility and the long-term stability of the performance, is beyond the scope of this work and will be presented in a forthcoming paper.

Parameter	Value
Entrance window	Pure Be, 50 μm
Drift gap thickness	10 mm
Transfer gap thickness	0.8 mm
Readout configuration	Chip on board
GEM pitch	50 μm
GEM hole diameter	30 μm
Gas filling	Pure DME @ 730 mbar

Table 2: Summary table of the basic properties of the GPD under test.

4. Electrical tests and working point definition

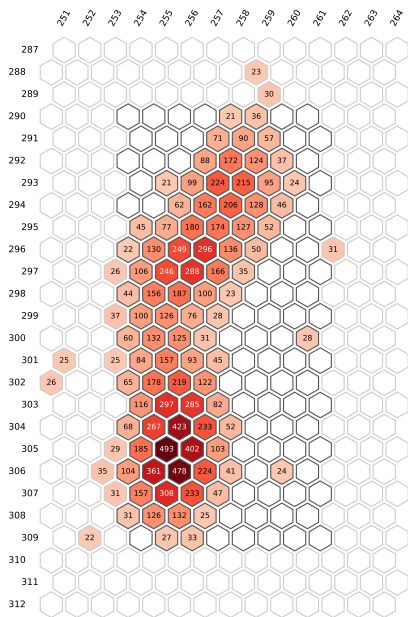


Figure 6: Display of a real XPOL-III track from a 5.9 keV radioactive ^{55}Fe source with a padding of three pixels on all four sides of the ROT. The indices on the top and left side of the ROI show the location on the readout matrix, while the text overlaid on the pixels represent the corresponding PHA value. Even a superficial comparison with Figure 3 reveals how, given the much lower trigger threshold, the vast majority of the track is now contained in the ROT, and the padding of three pixels used here is in fact very generous even for a typical high energy track.

This section describes the initial electrical and functional tests that we performed to verify the basic functionality of the ASIC and gauge the optimal working point, in terms of event padding and serial readout clock, to be used for measuring the relevant high-level performance metrics that we shall present in section 5. For completeness, Figure 6 shows a single event display of a real track from a 5.9 keV radioactive ^{55}Fe source, illustrating much of the improvements from the new trigger circuitry discussed in section 2.

4.1. Electronics Noise

As already explained, and unlike the previous XPOL generations, XPOL-III allows to set the coordinates of the ROI for the

readout externally, and we extensively used this novel feature to measure the system noise in a number of readout chips. More specifically, we use a series of partially overlapping, 21×21 regions of interest covering the entire active area of the chip and, for each ROI, we perform a number of readouts, with the same basic readout sequence used in nominal data-taking. For each pixel, the root mean square of the pedestal subtracted PHA values is a measure of the pre-amplifier noise¹

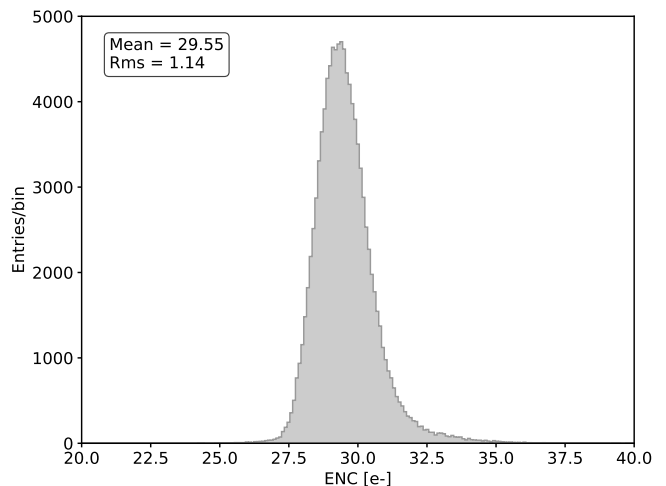


Figure 7: Noise distribution measured across the channels of a typical XPOL-III chip. The average noise is $\sim 30 e^-$ ENC.

Figure 7 shows the noise distribution measured across the channels of a typical XPOL-III chip. The average noise is about $30 e^-$ ENC. It should be emphasized that this level of noise, translating into a track S/N ratio of ~ 200 for a typical event, is largely irrelevant for our applications, and not a limiting factor in any practical sense.

We note that the initial chips manufactured at the foundry and tested for this work have a small fraction of a % dead channels; while this does not represent an issue for operating a GPD, a fine tuning of the manufacturing will be investigated with the foundry.

4.2. ROT Padding

We systematically investigated the effect of the ROT padding settings on the basic track properties by exploiting the hybrid XPOL-III operational mode described in section 2 and acquiring X-ray data with different, pre-loaded padding values—from 2 to 5 pixels on all four sides of the ROT. Since the main purpose of the padding is to guarantee the full containment of the electron track, we resorted to using *the fraction of events for which at least one of the pixels in the track lies on a border row or column*, which might indicate a possible track leakage, as the relevant metric for our study.

¹To be more precise, since we are operating with an online, event-by-event pedestal subtraction strategy as described in section 2, the raw rms values are a factor of $\sqrt{2}$ larger than the intrinsic noise of the amplifier. This scale factor is correctly accounted for in Figure 7 as well as in the numbers quoted in the text.

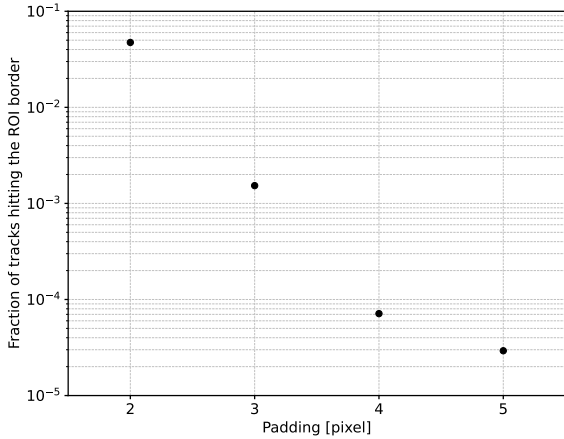


Figure 8: Fraction of events for which at least one of the pixels in the main track lies on the borders of the ROI, as a function of the ROT padding setting. The data points have been measured with a full irradiation of the detector with 5.9 keV photons from a ^{55}Fe radioactive source, with the zero suppression threshold set to $\sim 2\sigma$ of the noise.

As shown in Figure 8 the fraction of tracks with border pixels decreases monotonically as the padding increases, going from several % at 2 pixels to a few 10^{-5} at 5 pixels. We emphasize that a single pixel above threshold on one of the borders of the ROI does not necessarily imply that the track has been actually truncated, nor that the polarimetric information encoded by the reconstructed track direction has been compromised appreciably. We therefore conservatively take a padding value of 2 pixels as the smallest practically usable and we deem padding values larger than 4 pixels as overly large, as the plot in Figure 8 clearly indicates that the curve starts flattening (cf. Figure 4).

We note that more elaborated padding strategies (e.g., use different values on different sides of the ROT) might conceivably provide an additional measurable performance gain. The magnitude of the potential improvement can be gauged by noting that reducing the padding by one unit on one side provides a relative reduction of the ROI size by

$$\frac{\delta n}{n} \approx \frac{1}{\sqrt{n}}, \quad (2)$$

which is $\sim 7\%$ at a typical average ROI size of 200 pixels. Since investigating the effects of such fine tuning is beyond the scope of this paper, we shall take a constant, comfortable padding of 3 pixels as our nominal working point from now on, unless stated otherwise.

4.3. Readout Time

As explained in section 2.2, the average readout time per event can be parametrized as a linear function of the number of pixels in the ROI. Since, for any given X-ray energy, events come in a large variety of different topologies—depending on the depth of the absorption point and the initial emission direction, as well as the stochastic nature of the interaction processes—even photons from a monochromatic source will generate in the

detector ROIs of many different sizes and shapes. As a consequence, illuminating the detector with a X-ray source provides a simple mean to study the dead time per event as a function of the ROI size.

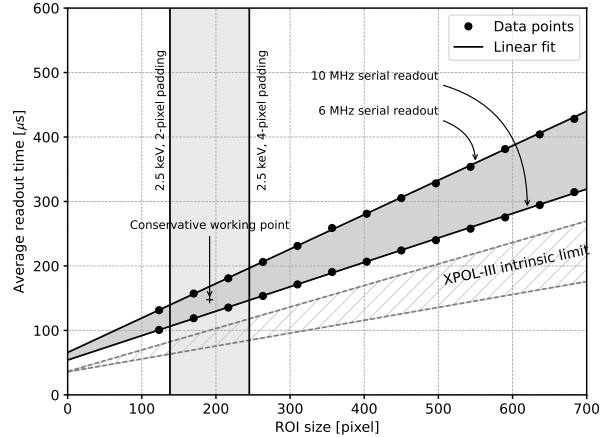


Figure 9: Readout time as a function of the ROI size, for two different values of the serial readout clock, obtained by illuminating the detector with 5.9 keV photons from a ^{55}Fe radioactive source, with a padding of 3 pixels on all four sides of the ROT. The solid lines represent the best linear fits to the data points for two different values (6 and 10 MHz) of the serial readout clock. The vertical gray band indicates the average ROI size that we expect at the reference energy of 2.5 keV for a padding of 2 and 4 pixels. The hatched region between the two dashed lines indicate the intrinsic XPOL-III readout limit (at 6 and 10 MHz readout clock), assuming that the pedestal subtraction is fully parallelized and in the ideal case where the back-end electronics did not introduce any additional delay to the readout sequence.

Figure 9 shows the measured readout time as a function of the ROI size for two different values of the serial readout clock (6 and 10 MHz), and a constant padding of 3 pixels on all four sides of the ROT, with the detector uniformly illuminated with 5.9 keV X-rays from a ^{55}Fe radioactive source. The data are fitted with the straight line in Equation (1). At our reference energy of ~ 2.5 keV, the center of our fiducial region in the padding vs readout clock phase-space yields a tentative working point of $\sim 150 \mu\text{s}$, at an average ROI size of ~ 200 pixels. This is to be compared with ~ 500 pixels and ~ 1 ms for the XPOL-I chip currently operating on PolarLight and IXPE.

We note that, due to the current design of our back-end electronics, the measured readout time includes a contribution of $\sim 35 \mu\text{s}$ for the pedestal subtraction in the FPGA, for a ROI of 200 pixels. For a high-throughput application, this component could be conceivably parallelized at the cost of a slight increase in the complexity of the system, yielding an additional $> 20\%$ increase in readout speed without side effects on any of the high-level performance metrics.

5. High-Level Performance Figures

In this section we briefly discuss the basic spectral and polarimetric response of the XPOL-III chip, embedded in the new GPD design. The reader should keep in mind that the readout ASIC is only a component of the mix, and the results are

dependent on a number of other factors, including the detector assembly, the characteristic of the filling gas, the amplification stage, as well as the track-reconstruction software. For the sake of internal consistency, all the tests described in the following are done at the working point identified in section 4, that is, with a constant padding of 3 pixels on the four sides of the ROT, and a serial readout clock of 7.5 MHz.

5.1. Energy Resolution

Figure 10 shows the pulse-height distribution in pure DME at the nominal data taking settings for a flat field with 5.9 keV photons from a ^{55}Fe radioactive source. After correcting for spatial non-uniformities of the GEM, we achieve a FWHM around 17%, in line with the corresponding figure for the IXPE flight detectors [3].

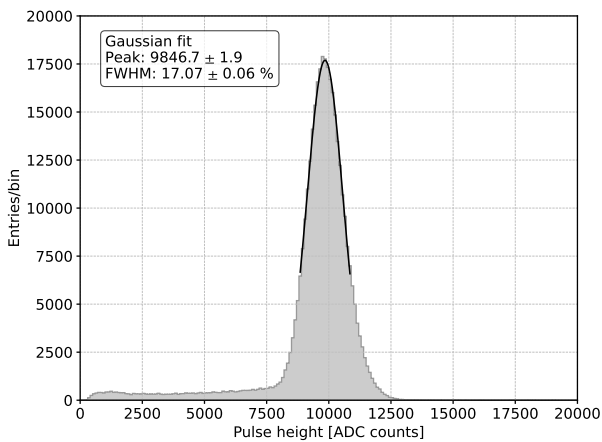


Figure 10: Spectrum of ^{55}Fe line with a gaussian fit in nominal working conditions. The detector surface is uniformly illuminated and the large-scale gain dis-uniformity of the Gas Electron Multiplier corrected.

We emphasize how even a superficial comparison with Figure 16 in [3] shows that the low-energy tail in the spectrum due to photon conversions in the passive materials is reduced by a factor ~ 2 , due to the elimination of the aluminum deposition on the inner face of the entrance window. While the suitability of a pure Be window for a long-term use in space will be investigated and presented in a separate paper, we note that this factor is beneficial for both the spectral deconvolution and the polarization measurement.

5.2. Azimuthal Response

We tested the azimuthal response of the GPD assembly with both unpolarized photons from a 5.9 keV ^{55}Fe radioactive source and polarized X-rays generated via Bragg diffraction at 45° on a graphite crystal. Our polarized setup produces three different monochromatic lines at 2.6, 5.2 and 7.8 keV, but the low- and high-energy ones are strongly suppressed due to the absorption in air and the energy dependence of the GPD quantum efficiency, respectively.

Figure 11 shows two modulation curves, measured in our unpolarized and polarized setups. For the latter, we selected events in the central 5.2 keV over a beam spot with a ~ 1 mm

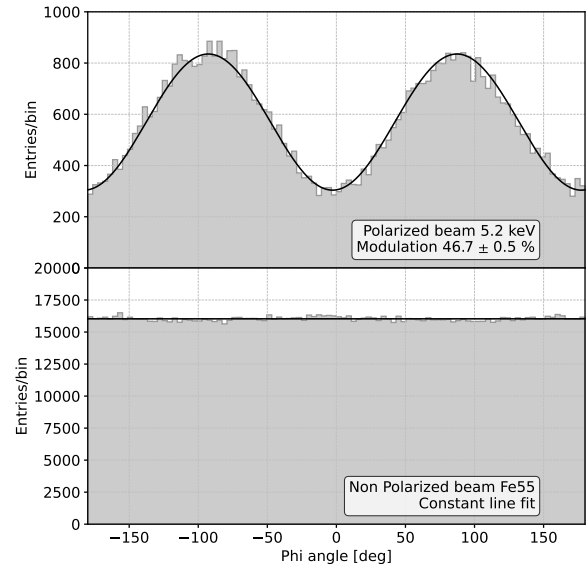


Figure 11: Measured modulation curve at 5.2 keV for a 100% polarized X-ray source. The modulation factor is 46.7% without any selection on the events, in line with previous measurements and with the prediction of our Monte Carlo simulation.

radius close to the center of the detector, and performing two separate acquisitions rotated by 90° in order to compensate for any possible residual systematic effect. (Although, as shown in the bottom panel, such effects are largely subdominant.) The measured modulation factor at 5.2 keV is $46.7 \pm 0.5 \%$, without any additional selection on the events other than that of the central line in the source spectrum. The measured spurious modulation at 5.9 keV is smaller than 1%, and, as explained in [3], is to be ascribed to the multiplication stage. This is in good agreement with both the figures for the IXPE focal-plane detectors (given the differences in the GPD assembly and the X-ray source) and with the prediction from our Monte Carlo simulations, indicating that the new readout chip is fully preserving the intrinsic polarimetric capabilities of the GPD.

6. Conclusions

We have developed and tested a new custom readout chip for high-throughput X-ray astronomical polarimetry. Compared to the ASIC currently operating on PolarLight and IXPE, XPOL-III is able to generate significantly smaller, and yet fully contained track images and to operate at a faster readout clock, with a streamlined readout sequence.

When combined, these factors reduce the average deadtime per event to $\sim 150 \mu\text{s}$, or a factor of 7 smaller than the current state of the art. Considering that at least $\sim 35 \mu\text{s}$ of the measured deadtime are an overhead introduced by the existing back-end electronics, a speed-up of a full order of magnitude is clearly within reach, making XPOL-III an ideal match for the upcoming generation of X-ray observatories.

This leap forward in readout speed is achieved with no measurable degradation in the polarimetric, spectral, imaging or

timing capability of the detector, as demonstrated by the tests presented in this work.

In addition, the reduction of at least a factor 2.5 of the ROI size is clearly very helpful in reducing the required bandwidth for both on board satellite operation as well for data transmission to the ground.

Finally, the possibility of operating at a trigger threshold as low as $\sim 150 e^-$ paves the way to new types of applications that were previously impossible, e.g., low-pressure configurations tailored to very low energies or, on the other side of the energy band, operating in pure ionization mode with suitable gas mixtures or other high efficiency, pixelated photon to charge converters.

We argue that this work constitutes a crucial step toward the deployment of a new generation of Gas Pixel Detectors matching the needs of future X-ray observatories. The development of suitable multiplications stages, free of systematic effects in the azimuthal response, is the other fundamental ingredient of the mix, and we shall report our progress in a separate paper.

7. Acknowledgements

This work was supported by the Italian Space Agency (ASI) through the agreements 2018-11-HH.O, “ADAM - Advanced Detectors for x-ray Astronomy Mission” and 2017.13-H0, “Italian participation to the NASA IXPE mission”

References

- [1] Hua Feng and et al. PolarLight: a CubeSat X-ray polarimeter based on the gas pixel detector. *Experimental Astronomy*, 47(1-2):225–243, April 2019.
- [2] Martin C. Weisskopf and et al. The imaging x-ray polarimetry explorer (ixpe): Pre-launch, 2021.
- [3] L. Baldini and et al. Design, construction, and test of the gas pixel detectors for the ixpe mission. *Astroparticle Physics*, 133:102628, 2021.
- [4] Costa E., Soffitta P., Bellazzini R., Brez A., Lumb N., and Spandre G. An efficient photoelectric x-ray polarimeter for the study of black holes and neutron stars. *Nature*, 411(6838):662 – 665, 2001. Cited by: 274.
- [5] R. Bellazzini, F. Angelini, L. Baldini, F. Bitti, A. Brez, M. Ceccanti, L. Latronico, M.M. Massai, M. Minuti, N. Omodei, M. Razzano, C. Sgrò, G. Spandre, E. Costa, and P. Soffitta. Reading a gem with a vlsi pixel ASIC used as a direct charge collecting anode. *Nuclear Instruments and Methods in Physics Research Section A: Accelerators, Spectrometers, Detectors and Associated Equipment*, 535(1):477 – 484, 2004. Proceedings of the 10th International Vienna Conference on Instrumentation.
- [6] R. Bellazzini, G. Spandre, M. Minuti, L. Baldini, A. Brez, F. Cavalca, L. Latronico, N. Omodei, M.M. Massai, C. Sgrò, E. Costa, P. Soffitta, F. Krummenacher, and R. de Oliveira. Direct reading of charge multipliers with a self-triggering CMOS analog chip with 105k pixels at 50 μ m pitch. *Nuclear Instruments and Methods in Physics Research Section A: Accelerators, Spectrometers, Detectors and Associated Equipment*, 566(2):552 – 562, 2006.
- [7] Robert A. Austin and Brian D. Ramsey. Optical imaging chamber for x-ray astronomy. *Optical Engineering*, 32(8):1990 – 1994, 1993.
- [8] S. N. Zhang and et al. eXTP: Enhanced X-ray Timing and Polarization mission. In Jan-Willem A. den Herder, Tadayuki Takahashi, and Marshall Bautz, editors, *Space Telescopes and Instrumentation 2016: Ultraviolet to Gamma Ray*, volume 9905, pages 505 – 520. International Society for Optics and Photonics, SPIE, 2017.
- [9] M. Barbanera, S. Citraro, C. Magazzù, A. Manfreda, M. Minuti, H. Nasimi, and C. Sgrò. Initial tests and characterization of the readout electronics for the ixpe mission. *IEEE Transactions on Nuclear Science*, 68(5):1144–1151, 2021.